Accurate and Precise Time-Delay Estimation for Ultrasound Elastography with Pre-Beamformed Channel Data

Morteza Mirzaei, Amir Asif and Hassan Rivaz

***Abstract*—Free-hand palpation ultrasound elastography is a non-invasive approach for detecting pathological alteration in tissue. In this method, the tissue is compressed by a hand-held probe and displacement of each sample is estimated, a process which is also known as Time delay estimation (TDE). Even with the simplifying assumption that ignores out of plane motion, TDE is an ill-posed problem requiring estimation of axial and lateral displacement for each sample from its intensity. A well-known class of methods for making elastography a well-posed problem is regularized optimization based methods which imposes smoothness regularization in the associated cost function. Herein, we propose to utilize channel data that has been compensated for time-gain and time-delay (introduced by transmission) instead of post-beamformed radio frequency (RF) data in the optimization problem. We name our proposed method CGLUE (Channel data for GLobal Ultrasound Elastography). We analytically derive bias and variances of TDE as functions of data noise for CGLUE and Global Ultrasound Elastography (GLUE) [1], and use the Cauchy Schwarz inequality to prove that CGLUE provides a TDE with lower bias and variance error. To further illustrate the improved performance of CGLUE, results of simulation, experimental phantom and *ex-vivo* experiments are presented.**

***Index Terms*—Ultrasound elastography, Time delay estimation (TDE), Regularized optimization, Channel data.**

I. Introduction

Elastography is a technique to detect pathological tissue alterations by extracting mechanical properties of the tissue. Elastography can be performed on different imaging modalities like magnetic resonance imaging [2], [3] and Ultrasound [4], [5]. Unlike biopsy that is invasive and considers a small portion of tissue, elastography is a non-invasive technique that considers the entire tissue and reduces the probability of missing abnormalities.

Ultrasound Elastography (USE) is an approach for detecting mechanical properties of tissue by taking advantage of ultrasound imaging. Ultrasound as an imaging tool has emerged in the latter half of the 20th century and has become one of the most popular imaging modalities [6]. The main advantages of ultrasound imaging lie in its noninvasive nature, low cost, convenience, and wide availability. USE helps in early diagnostics which substantially increases the success probability of treatment. In recent years, USE has been explored for several clinical applications including ablation guidance and monitoring [7], differentiating benign thyroid nodules from malignant ones [8]–[10] and breast lesion characterization [11]–[13]. Surgical treatment of liver cancer [14]–[16], assessment of non-alcoholic fatty liver disease [17], assessment of fibrosis in chronic liver diseases (CLD) [18], [19], detecting prostate cancer [20], [21], differentiating abnormal lymph nodes in benign conditions [22] and brain tumor surgery [23], [24] are other relevant clinical applications of USE.

The base of elastography is the relation between stiffness change and pathological changes. The scatterers of tissue are displaced by external stimuli or internal forces (the pumping action of the heart) and shear modulus or Young's modulus can be calculated by estimating tissue motion and solving an inverse problem [25], [26].

Different classifications for USE are proposed in the literature, however it can be broadly grouped into dynamic and quasi-static elastography. Dynamic methods, such as shear wave imaging (SWI) [27], [28] and acoustic radiation force imaging (ARFI) [29], [30], use Acoustic Radiation Force (ARF) to generate displacement in the tissue. Transient elastography is another common dynamic method in which low frequency vibrations are applied to tissue [31]. These methods can be used to estimate quantitative mechanical properties of tissue. However for quasi-static elastography, excitation is performed by simply pressing an ultrasound probe against tissue [4], [32] which can be done by utilizing a robotic arm [33], [34] or a hand-held probe (i.e. free-hand palpation) [35], [36]. Another approach is to use the ablation probe to generate displacements [37]. In this paper, we focus on quasi-static free-hand palpation USE and compress the tissue along the axial direction, which inevitably creates deformation in both lateral and out of plane directions.

The problem of displacement estimation is ill-posed since the intensity of one sample provides one equation. Most biological tissues are nearly incompressible, i.e., the volume of the tissue does not change by compressing it. Therefore, axial compression will also lead to lateral and out of plane deformations. Even after neglecting out of plane motion, each sample moves in two directions which results in two unknown variables, and two unknowns cannot be uniquely determined from one equation [38]. To make the problem a well-posed one, different methods for quasi-static elastography are proposed in the literature, which in turn can be broadly categorized into window-based and regularized optimization-based approaches. In the window-based methods, few samples

Morteza Mirzaei, Amir Asif and Hassan Rivaz are with the Department of Electrical and Computer Engineering, Concordia University, Montreal, QC, H3G 1M8, Canada. Email: m_irzae@encs.concordia.ca , amir.asif@concordia.ca and hrivaz@ece.concordia.ca

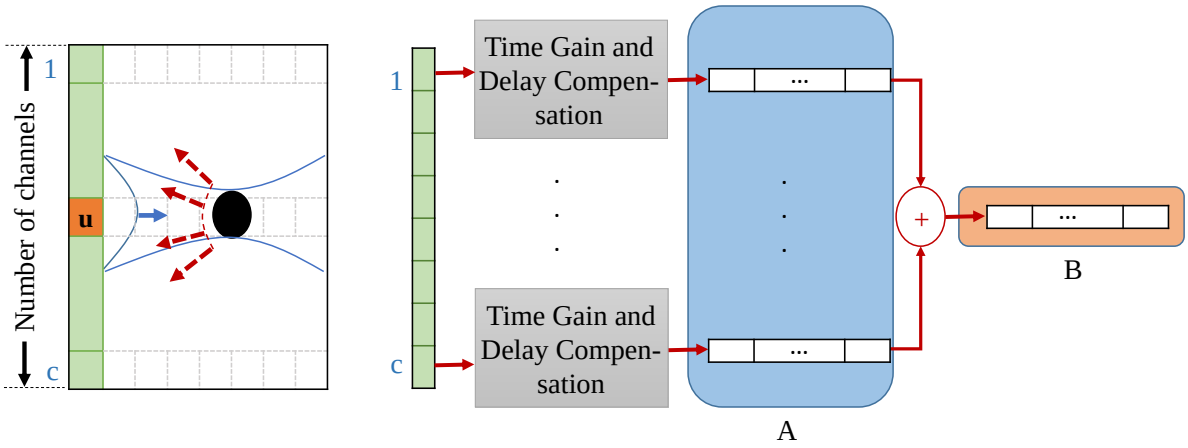

Fig. 1: For transmitted focused beam in line 'u', all of reflected data (shown in red dashed-arrows) are amplified to compensate time-gain. The time-delays due to transmission are also compensated. By summation of time-gain and time-delay compensated data (shown in section 'A'), the corresponding RF line of element 'u' is generated as shown in section 'B'. Instead of considering one RF line (shown in section 'B'), we consider all information of section 'A' in CGLUE.

are considered around the reference sample. A corresponding group of samples with similar sample values in the following image is located and displacement of these two groups is represented as the displacement of the reference sample. Several similarity metrics are used to locate the corresponding window such as maximization of the normalized cross correlation (NCC) of windows [39]–[41], phase-correlation wherein zero crossing of phase determines displacement [42], sum of absolute difference of windows [43] and deep learning based techniques [44]–[47]. Another approach for making the USE well-posed is imposing smoothness regularization in optimizing a regularized cost function [48]–[53]. These methods are computationally complex, but real-time USE based on regularized cost functions have recently been developed by exploiting Dynamic Programming and Analytic Minimization (DPAM) [54], [55] and GLobal Ultrasound Elastography (GLUE) [1]. Combination of window-based approaches and regularized optimization method has recently been proposed in [56] to take advantages of both methods.

To the best of authors knowledge, all previously developed methods use RF or B-mode data for TDE. In this paper, we propose to use pre-beamformed channel data. An ultrasound image comprises of multiple scan lines (RF lines). For generating each line, an array of transducers transmit the acoustic energy pulse while timing the piezoelectric crystals to focus the beam (as shown with blue curves in Fig.1). Reflections are collected by the same piezoelectric crystals and digitized. Based on the classic Nyquist-Shannon sampling theorem, the sampling rate must be at least twice the bandwidth, in order to avoid aliasing [57]. Time gain and time-delay due to transmission are compensated for the sampled data (i.e, channel data) as shown in part A of Fig. 1. By integrating data, a RF line is generated as shown in part B of Fig. 1. TDE is often performed using RF data, however in this paper we use time-gain and time-delay corrected channel data (shown in section A of Fig. 1) instead of RF data (shown in section B of Fig. 1). We name our method as Channel data for GLobal Ultrasound Elastography (CGLUE) and prove that the error of estimated displacement with CGLUE is less than GLUE. The initial results of the proposed method based solely on experimental results has been published in [58]. This paper makes additional contributions by analytically verifying the superiority of CGLUE and presenting results from comprehensive simulations, ex-vivo, and phantom experiments.

II. METHODS

Let I_1 and I_2 of size (m, n, c) be two sets of time-gain and time-delay compensated channel data collected as the tissue undergoing some deformation. I_{1b} and I_{2b} of size (m, n) are the corresponding beam-formed RF data. In these data sets, m and n are depth and width of the imaged tissue and c is the number of channels that receive the reflected data. The goal of TDE is estimating the displacement field between these two data sets. In this section, we first briefly review our previous work, GLUE [1], and then present CGLUE. More importantly, we derive an analytically proof of the superiority of CGLUE over GLUE by comparing the error for the estimated TDEs. In GLUE and CGLUE, the displacements are estimated in two steps as integer and subsample displacement estimates. The initial integer displacement estimates come from Dynamic Programming (DP), which is a recursive optimization based method for image registration. In this method, different integers are nominated for displacement of each RF sample. The cost function incorporates similarity of RF samples and displacement continuity and optimizing this cost function leads to integer displacement of RF samples [54].

A. GLUE: GLobal Ultrasound Elastography

The goal of GLUE is to calculate the subsample displacement part by minimizing the following cost function:

$$C(\Delta a_{11}, \Delta l_{11}, \ldots, \Delta a_{mn}, \Delta l_{mn}) = \sum_{j=1}^{n} \sum_{i=1}^{m} \{D(i, a_{ij}, \Delta a_{ij}, j, l_{ij}, \Delta l_{ij}) + R(i, a_{ij}, \Delta a_{ij}, j, l_{ij}, \Delta l_{ij})\} \quad (1)$$

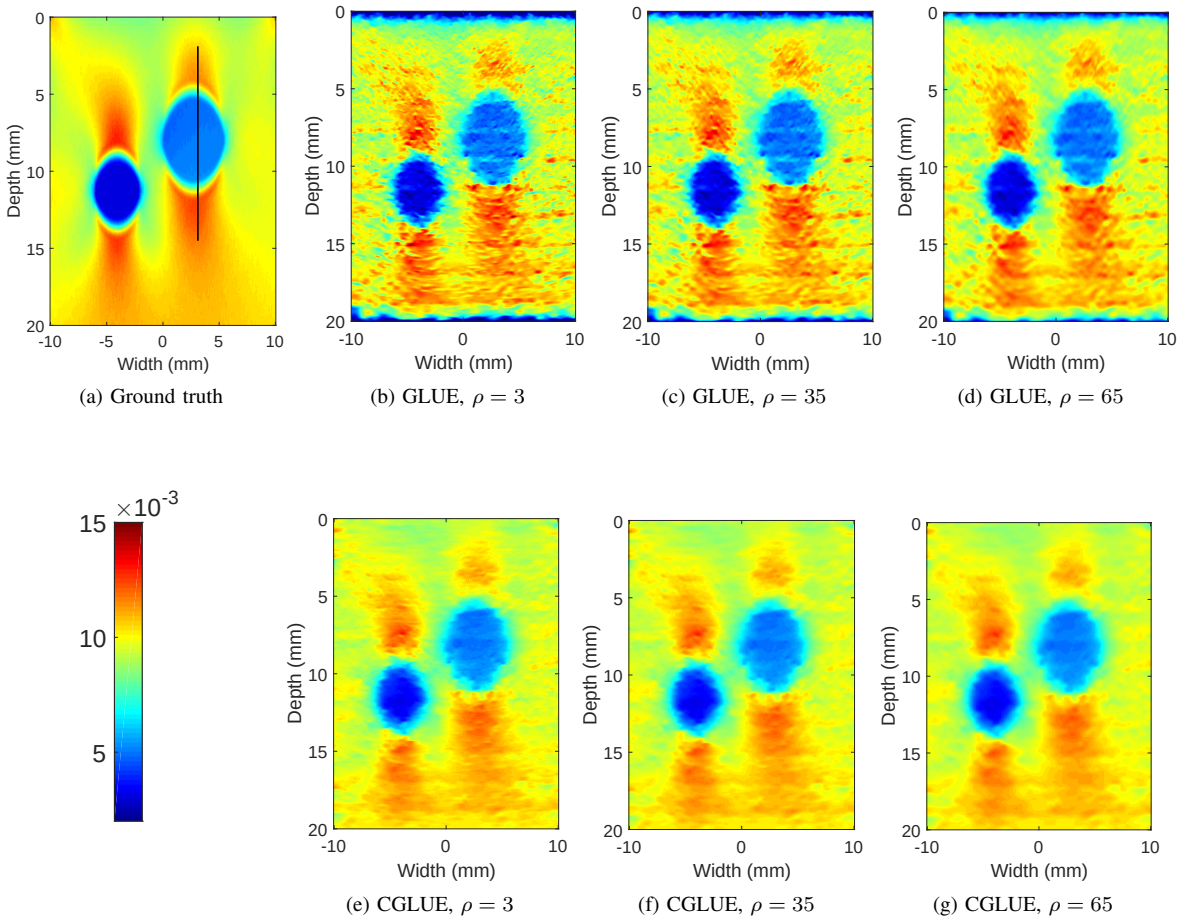

(a) Ground truth (b) GLUE, $\rho = 3$ (c) GLUE, $\rho = 35$ (d) GLUE, $\rho = 65$

(e) CGLUE, $\rho = 3$ (f) CGLUE, $\rho = 35$ (g) CGLUE, $\rho = 65$

Fig. 2: Strain images of the simulation phantom calculated using GLUE and CGLUE. The ground truth is shown in (a). Results of GLUE with different data sizes considered for LSQ are illustrated in (b)-(d). Results of CGLUE with different data sizes considered for LSQ are also illustrated in (e)-(g). Note that the CGLUE result in (e) is less noisy despite a small value for ρ.

where the data term D is:

$$D(i, a_{ij}, \Delta a_{ij}, j, l_{ij}, \Delta l_{ij}) = [I_{1b}(i,j) - I_{2b}(i + a_{ij} + \Delta a_{ij}, j + l_{ij} + \Delta l_{ij})]^2 \quad (2)$$

and the regularization term R is:

$$\begin{aligned} R(i, a_{ij}, \Delta a_{ij}, j, l_{ij}, \Delta l_{ij}) = \\ \alpha_1(a_{ij} + \Delta a_{ij} - a_{i-1j} - \Delta a_{i-1j})^2 \\ +\alpha_2(a_{ij} + \Delta a_{ij} - a_{ij-1} - \Delta a_{ij-1})^2 \\ +\beta_1(l_{ij} + \Delta l_{ij} - l_{i-1j} - \Delta l_{i-1j})^2 \\ +\beta_2(l_{ij} + \Delta l_{ij} - l_{ij-1} - \Delta l_{ij-1})^2. \end{aligned} \quad (3)$$

In these equations, I_{1b} and I_{2b} are pre- and post- compressed beam-formed RF data of size $m \times n$. The symbols a_{ij} and l_{ij} are axial and lateral integer displacements for sample (i, j) that are estimated by DP while Δa_{ij} and Δl_{ij} are subsample axial and lateral displacements that should be calculated. Finally, α_1, α_2, β_1 and β_2 are regularization parameters.

In the next section, CGLUE is proposed that modifies the data term by utilizing channel data instead of beam-formed data.

B. CGLUE: Channel data for GLobal Ultrasound Elastography

By considering pre-beamformed channel data, the data term of Eq. (2) is replaced by

$$D(i, a_{ij}, \Delta a_{ij}, j, l_{ij}, \Delta l_{ij}) = \frac{1}{c} \sum_{k=1}^{c} \Big(I_1(i,j,k) - I_2(i + a_{ij} + \Delta a_{ij}, j + l_{ij} + \Delta l_{ij}, k) \Big)^2.$$

Optimizing the cost function based on the proposed data term is not a trivial problem due to nonlinearity of I_2. To linearize I_2 with respect to unknown variables, we replace $I_2(i + a_{ij} + \Delta a_{ij}, j + l_{ij} + \Delta l_{ij}, k)$ with its first order Taylor series expansion around $(i + a_{ij}, j + l_{ij}, k)$. Furthermore, to simplify the notation, we denote $I_2(i + a_{ij}, j + l_{ij}, k)$ as $I_2(.)$, so the data term can be rewritten as

$$D(i, a_{ij}, \Delta a_{ij}, j, l_{ij}, \Delta l_{ij}) = \frac{1}{c} \sum_{k=1}^{c} \Big(I_1(i,j,k) - I_2(.) - \Delta a_{ij} I'_{2a}(.) - \Delta l_{i,j} I'_{2l}(.) \Big)^2 \quad (4)$$

where $I'_{2a}(.)$ and $I'_{2l}(.)$ are derivatives of I_2 in the axial and lateral directions, respectively.

The regularization term in Eq. (3) reduces estimation variance at the cost of increased bias by penalizing the difference between $a_{ij}+\Delta a_{ij}$ and $a_{i-1j}-\Delta a_{i-1j}$, which leads to an underestimated displacement estimation. Therefore, as proposed in [55], [56], we consider ε_a and ε_l in the regularization term, where ε_a is the average of integer axial displacement difference between subsequent samples i and $i-1$ and ε_l is the average of integer lateral displacement difference between samples j and $j-1$ which are available from DP. Therefore, the regularization term can be modified as

$$\begin{aligned} R(i,a_{ij},\Delta a_{ij},j,l_{ij},\Delta l_{ij}) = \\ &\alpha_1(a_{ij}+\Delta a_{ij}-a_{i-1j}-\Delta a_{i-1j}-\varepsilon_a) \\ &+\alpha_2(a_{ij}+\Delta a_{ij}-a_{ij-1}-\Delta a_{ij-1}) \\ &+\beta_1(l_{ij}+\Delta l_{ij}-l_{i-1j}-\Delta l_{i-1j}) \\ &+\beta_2(l_{ij}+\Delta l_{ij}-l_{ij-1}-\Delta l_{ij-1}-\varepsilon_l). \end{aligned} \tag{5}$$

By considering the cost function C as a summation of data and regularization terms that are proposed in Eqs. (4) and (5), differentiating it with respect to Δa_{ij} and Δl_{ij}, and stacking all $2mn$ unknown parameters in a vector as

$$\Delta d_{2m\times n} = [\Delta a_{11}, \Delta l_{11}\Delta a_{12}, \Delta l_{12}, \cdots, \Delta a_{mn}, \Delta l_{mn}]^{\mathrm{T}},$$

we have

$$\underbrace{(H+V)}_{X}\Delta d = \underbrace{\frac{1}{c}\sum_{k=1}^{c}(P\mu)-Vd-b\otimes\begin{bmatrix}\varepsilon_a\\ \varepsilon_l\end{bmatrix}}_{y}, \tag{6}$$

where X and y are two known matrices, $\otimes$ is Kronecker tensor product and Δd can be calculated by the lower-upper (LU) decomposition (e.g. the $X\backslash y$ command in MATLAB). Details of the matrix X and the vector y are provided in the appendix.

C. Error Analysis

To analytically compare the errors of GLUE and CGLUE, we derive equations for the error of TDE as functions of noise in the data. Let $\hat{d}_{ij}=(\hat{a}_{ij},\hat{l}_{ij})$ denote the ground truth displacement of sample (i,j). For simplicity of mathematical derivations, we assume that the motion is only in the axial direction and $\hat{l}_{ij}=0$ without loss of generality. Also by assuming the ultrasound noise to be an additive noise [59], [60], the data at sample (i,j,k) is

$$\begin{aligned} I_1(i,j,k) &= \hat{I}(i,j,k)+n_1(i,j,k) \\ I_2(i,j,k) &= \hat{I}(i-\hat{a}_{ij},j,k)+n_2(i,j,k) \end{aligned} \tag{7}$$

where $n_1(i,j,k)$ and $n_2(i,j,k)$ can have any distribution with expected values of μ_1,μ_2 and variances of σ_1,σ_2. In this section we denote the estimated displacements as a_{ij} and l_{ij}, which represent summation of integer and subsample displacements.

1) GLUE error: In beamforming the channel data corresponding to one element, the collected data with different channels should be time-delayed and time-gained with respect to their spatial distances from the element. The beamformed data is generated by adding the time-delayed and time-gained data across all channels. Since time-delay and time-gain compensation are linear operations and as such do not change the distribution of noise, therefore we consider beamforming as summation of channel data as follows

$$\begin{aligned} I_{1b}(i,j) &= \sum_{k=1}^{c} I_1(i,j,k) = \sum_{k=1}^{c}\hat{I}(i,j,k)+n_1(i,j,k) \\ I_{2b}(i,j) &= \sum_{k=1}^{c} I_2(i,j,k) = \sum_{k=1}^{c}\hat{I}(i-\hat{a}_{i,j},j,k)+n_2(i,j,k). \end{aligned} \tag{8}$$

The cost function for GLUE can be written as

$$\begin{aligned} C &= \sum_{j=1}^{n}\sum_{i=1}^{m}\Big(I_{1b}(i,j)-I_{2b}(i+a_i,j)\Big)^2 \\ &= \sum_{j=1}^{n}\sum_{i=1}^{m}\Bigg[\sum_{k=1}^{c}\Big(\hat{I}(i,j,k)+n_1(i,j,k) \\ &\qquad -\hat{I}(i+a_{ij}-\hat{a}_{ij},j,k)-n_2(i+a_{ij},j,k)\Big)\Bigg]^2+R. \end{aligned} \tag{9}$$

By applying the first order Taylor series approximation for nonlinear functions, we have

$$\begin{aligned} C = \sum_{j=1}^{n}\sum_{i=1}^{m}\Bigg[\sum_{k=1}^{c}\Big(&\hat{I}(i,j,k)+n_1(i,j,k)-\hat{I}(i,j,k) \\ &-(a_{ij}-\hat{a}_{ij})\hat{I}'_a(i,j,k)-n_2(i+a_{ij},j,k)\Big)\Bigg]^2+R. \end{aligned} \tag{10}$$

By differentiating the cost function and setting the derivative to zero, we have

$$a_{ij} = \hat{a}_{ij}+\frac{\sum_{k=1}^{c} n_1(i,j,k)-n_2(i+a_{ij},j,k)}{\sum_{k=1}^{c}\hat{I}'_a(i,j,k)}. \tag{11}$$

The expected value and variance of the $a_{i,j}$ at sample (i,j) are

$$\begin{aligned} E_g[a_{ij}] &= \hat{a}_{ij}+\frac{c(\mu_1-\mu_2)}{\sum_{k=1}^{c}\hat{I}'_a(i,j,k)} \\ var_g[a_{ij}] &= \frac{c(\sigma_1+\sigma_2)}{\Big(\sum_{k=1}^{c}\hat{I'}_a(i,j,k)\Big)^2}. \end{aligned} \tag{12}$$

2) CGLUE error: Considering Eq. (7), the cost function of CGLUE is

$$\begin{aligned} C &= \frac{1}{c}\sum_{j=1}^{n}\sum_{i=1}^{m}\sum_{k=1}^{c}\Big(I_1(i,j,k)-I_2(i+a_{ij},j,k)\Big)^2+R \\ &= \frac{1}{c}\sum_{j=1}^{n}\sum_{i=1}^{m}\sum_{k=1}^{c}\Big(\hat{I}(i,j,k)+n_1(i,j,k) \\ &\qquad -\hat{I}(i+a_{ij}-\hat{a}_{ij},j,k)-n_2(i+a_{ij},j,k)\Big)^2\Big) \end{aligned} \tag{13}$$

Following the same approach as the one used in section $C.1$ for estimating the displacement, we have

$$a_{ij} = \hat{a}_{ij}+\frac{\sum_{k=1}^{c}\hat{I}'_a(i,j,k)\Big(n_1(i,j,k)-n_2(i+a_{ij},j,k)\Big)}{\sum_{k=1}^{c}\hat{I}'^2_a(i,j,k)}. \tag{14}$$

The expected value and variance of the a_{ij} are

$$\begin{aligned} E_c[a_{ij}] &= \hat{a}_{ij} + \frac{(\mu_1-\mu_2)\sum_{k=1}^{c}\hat{I}'_a(i,j,k)}{\sum_{k=1}^{c}\hat{I}'^2_a(i,j,k)} \\ var_c[a_{ij}] &= \frac{\sigma_1+\sigma_2}{\sum_{k=1}^{c}\hat{I}'^2_a(i,j,k)}. \end{aligned} \tag{15}$$

3) Statistical error analysis: To compare the expected values and variances, we rewrite $(\sum_{k=1}^{c}\hat{I'}_a(i,j,k))^2$ as $(\mathbf{1}.\hat{I'}_a(i,j))^2$ where $\mathbf{1}$ and $\hat{I'}_a(i,j)$ are vectors of size $1\times c$ as $\mathbf{1}=[1,\ldots,1]$ and $\hat{I'}_a(i,j)=[\hat{I'}_a(i,j,1),\ldots,\hat{I'}_a(i,j,c)]$. The operator '.' is the inner product of the two vectors. According to Cauchy Schwarz inequality we have

$$\begin{aligned} \Big(\sum_{k=1}^{c}\hat{I'}_a(i,j,k)\Big)^2 &= \Big(\mathbf{1}.\hat{I'}_a(i,j)\Big)^2 \\ &\le \Big(\sum_{k=1}^{c}1^2\Big)\Big(\sum_{k=1}^{c}\hat{I}'^2_a(i,j,k)\Big) \\ &= c\sum_{k=1}^{c}\hat{I}'^2_a(i,j,k), \end{aligned} \tag{16}$$

therefore

$$\begin{aligned} E_c[a_{ij}] = \hat{a}_{ij} + \frac{(\mu_1-\mu_2)\sum_{k=1}^{c}\hat{I}'_a(i,j,k)}{\sum_{k=1}^{c}\hat{I}'^2_a(i,j,k)} \le \hat{a}_{ij} \\ + \frac{c(\mu_1-\mu_2)}{\sum_{k=1}^{c}\hat{I}'_a(i,j,k)} = E_g[a_{ij}]. \end{aligned}$$

and also

$$\begin{aligned} var_c[a_{ij}] = \frac{\sigma_1+\sigma_2}{\sum_{k=1}^{c}\hat{I}'^2_a(i,j,k)} \le \quad \frac{c(\sigma_1+\sigma_2)}{\Big(\sum_{k=1}^{c}\hat{I'}_a(i,j,k)\Big)^2} \\ = var_g[a_{ij}]. \end{aligned}$$

D. Data Acquisition

In this section, the data that is utilized in different experiments of the paper are described and then results of CGLUE are compared with GLUE in Results Section to illustrate improved performance of the CGLUE. For phantom and *ex-vivo* data where ground truth is not known, the bias and variance of the error cannot be compared quantitatively. However, we know that the strain maps should not have large fluctuations in a homogeneous medium as shown in the FEM and analytical strain maps. For the sake of comparison, the CNR is used to provide a quantitative mean for assessing the proposed method according to [61]

$$\text{CNR} = \frac{2(\bar{s}_b-\bar{s}_t)^2}{\sigma_b^2+\sigma_t^2}, \tag{17}$$

where $\bar{s}_t$ and $\bar{s}_b$ are the spatial strain averages of the target and background, σ_b^2 and σ_t^2 are the spatial strain variances of the target and background, respectively [62].

For estimating the axial strain, the displacement field should be differentiated. To reduce noise effect of differentiating, it is common to use least square estimation (LSQ) for strain estimating. For estimating strain of each sample, a few neighboring samples in a window of size ρ are considered and a line is fitted to their displacements. The tangent of the line is considered as the strain for the middle sample. Considering more data points for least square makes the strain smooth at the cost of losing resolution. For each experiment, three different window sizes are utilized for least square estimation to illustrate the superior performance of the CGLUE.

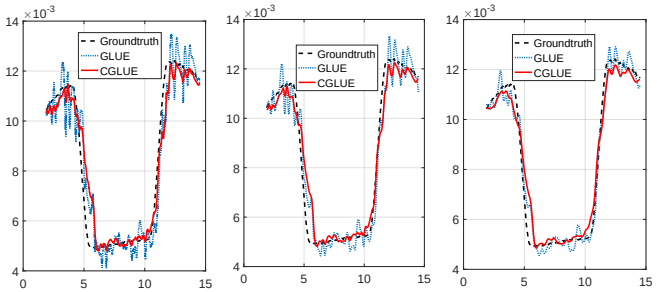

(a) $\rho = 3$ (b) $\rho = 35$ (c) $\rho = 65$

Fig. 3: Strain profiles of the simulated phantom across the vertical line in Fig. 2(a) calculated by GLUE and CGLUE. Windows of length 3, 35 and 65 are used for estimating strain by LSQ in (a), (b) and (c), respectively.

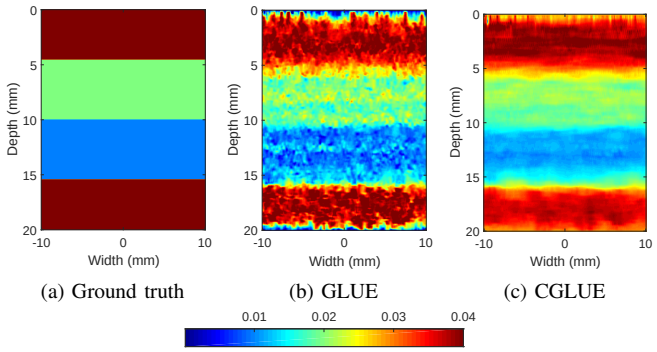

(a) Ground truth (b) GLUE (c) CGLUE

Fig. 4: Ground truth strain of the simulated phantom is shown in (a). Estimated strains by GLUE and CGLUE are shown in (b) and (c), respectively.

Simulation Data

A simulated phantom is generated by utilizing the Field II ultrasound simulation software [63], [64] by randomly distributing slightly more than 10 scatterers per mm^3 to satisfy the Rayleigh scattering regime. The simulated phantom is homogeneous with a Young's modulus of 16 kPa. Two cylindrical inclusions with Young's modulus of 40 kPa and 70 kPa are included in the phantom. For compressing the phantom and computing its ground truth displacement, FEM-based deformations are computed using the ABAQUS software package (Johnston, RI, USA) with mesh size of 0.05 mm^2. It

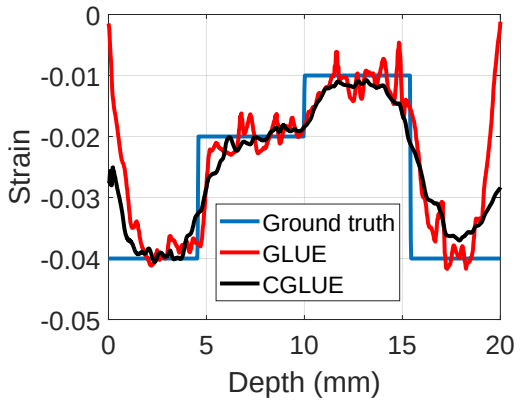

(a)

Fig. 5: Strain profiles of the simulated uniform phantom across a vertical line, calculated by GLUE and CGLUE.

TABLE I: Bias and variance of strain estimation error for GLUE and CGLUE with different levels of noise for FEM simulation study. For each level of noise the experiment is repeated 100 times and the reported values in this table are averages of the 100 experiments.

SNR (dB)		Bias	Variance
∞	GLUE	-28.23×10^{-5}	10.69×10^{-7}
	CGLUE	-7.14×10^{-5}	3.12×10^{-7}
40	GLUE	-28.95×10^{-5}	10.81×10^{-7}
	CGLUE	-7.2×10^{-5}	3.2×10^{-7}
30	GLUE	-29.2×10^{-5}	10.97×10^{-7}
	CGLUE	-7.3×10^{-5}	3.21×10^{-7}
25	GLUE	-41.2×10^{-5}	11.04×10^{-7}
	CGLUE	-14.3×10^{-5}	3.4×10^{-7}

should be mentioned that we had to interpolate the position of scatterers to generate the ground truth for the deformed digital phantom. However, this interpolation itself can introduce bias and variance, which is inevitable for any FEM simulation. Therefore, to overcome this issue, we have simulated another phantom with four uniform layers wherein the displacements can be calculated analytically (without FEM) with Poisson ratio of 0.49 to test the validity of the results of GLUE and CGLUE. Ultrasound images are simulated utilizing the Field II software. The probe consists of 192 elements with width of 0.22 mm and height of 5 mm for each element and also kerf of 0.05 mm. For each transmission, the reflected data is recorded by 64 channels. The center and sampling frequencies are 8 MHz and 100 MHz, respectively.

Phantom Data

The phantom data is acquired from a tissue mimicking breast phantom (059 tissue mimicking breast phantom, CIRS tissue simulation & phantom technology, Norfolk, VA, USA) using an E-Cube R12 ultrasound machine (Alpinion, Bothell, WA, USA) with a L3-12H probe at the center frequency of 11.5 MHz and sampling frequency of 40 MHz.

Ex-vivo Data

To highlight the improved performance of CGLUE, an *ex-vivo* experiment is organized by placing a small piece of olive in a lamb liver. We purchased a fresh liver from a local butcher and made a very small hole in the liver. We then inserted a small piece of olive with roughly size of $(10\times5\times5)$ mm^3 into the liver through the hole. The data are collected by E-Cube R12 ultrasound machine (Alpinion, Bothell, WA, USA) with a L3-12H probe at the center frequency of 11.5 MHz and a sampling frequency of 40 MHz.

III. Results

Simulation Results

The time delay profile for the simulated phantom is estimated by GLUE and CGLUE and the strain is estimated by the LSQ method for windows of lengths 3, 35 and 65. As shown in Fig. 2, CGLUE exhibits substantially better performance in all scenarios.

To provide a better comparison, we illustrate the Edge Spread Function (ESF) of the estimated strains across a vertical line shown in Fig. 2 (a). As it is clear form Fig. 3, the ESF of the CGLUE is closer to the ground truth as compared to GLUE in all cases. The noticeable point is that the estimated strain by CGLUE with $\rho = 3$ is smooth, however, the result of GLUE for $\rho = 3$ has much more fluctuations and increasing ρ has a significant smoothing effect on the estimated strain. We also have added different levels of noise to channel data and have calculated bias and variance of the strain estimation error based on the following formulas

$$\begin{aligned} \text{Bias} &= \frac{\sum_{i=1}^{m}\sum_{j=1}^{n} S_e(i,j) - S_g(i,j)}{m\times n}, \\ \text{Variance} &= \frac{\sum_{i=1}^{m}\sum_{j=1}^{n} (S_e(i,j) - S_g(i,j))^2}{m\times n} - \text{Bias}^2, \end{aligned} \tag{18}$$

where S_e and S_g are estimated and ground truth strains and m, n are axial and lateral size of data. Table I shows bias and variance of estimation error for different levels of noise and different methods. For each level of noise, we have repeated the experiment 100 times and the results are reported in Table I.

The estimated strain profiles for the simulated phantom with four uniform layers are shown in Fig. 4. ESFs across a vertical line are also shown in Fig. 5 which verify a low bias and a low variance of the TDE error corresponding to CGLUE and GLUE.

Similar to the previous experiment, we have added different levels of noise to the channel data and have calculated bias and variance of the strain error according to Eq. 18. Table II shows bias and variance of estimation error for GLUE and CGLUE with different levels of noise. For each level of noise, we have repeated the experiment 100 times and the results are reported in Table II.

Phantom Results

The strain of phantom data is illustrated in Fig.6. Three different windows are considered for LSQ with sizes of 3, 35

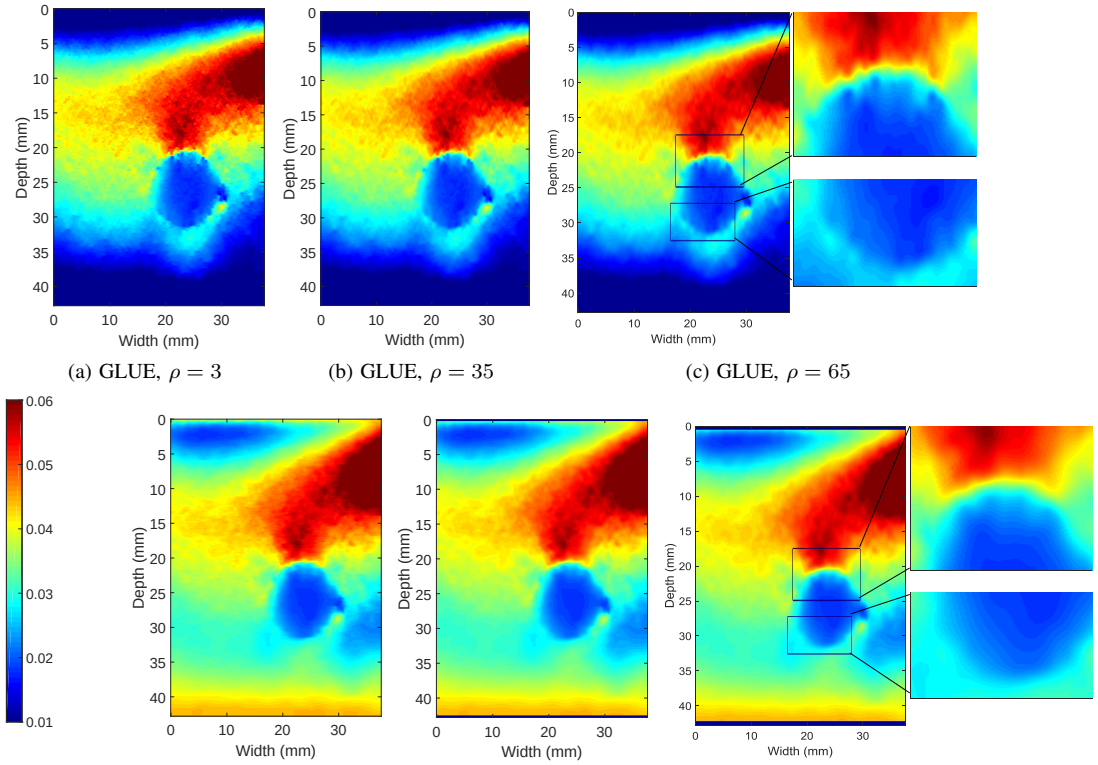

(a) GLUE, $\rho = 3$ (b) GLUE, $\rho = 35$ (c) GLUE, $\rho = 65$

(d) CGLUE, $\rho = 3$ (e) CGLUE, $\rho = 35$ (f) CGLUE, $\rho = 65$

Fig. 6: Strain images of the tissue mimicking phantom calculated using GLUE and CGLUE. The B-mode image is shown in (a). Strain fields calculated by GLUE for different LSQ window sizes are illustrated in (b)-(d). Strain fields calculated by CGLUE for different LSQ window sizes are also illustrated in (e)-(g). Note that the CGLUE result in (e) is less noisy despite a small value for ρ.

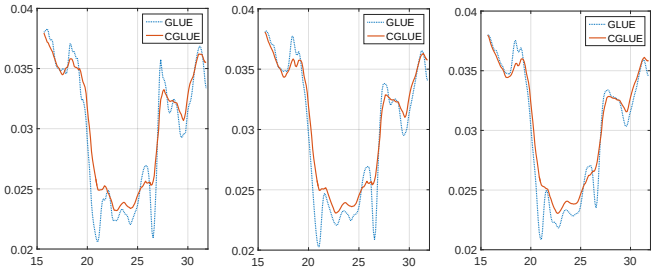

(a) $\rho = 3$ (b) $\rho = 35$ (c) $\rho = 65$

Fig. 7: Strain profiles of the tissue mimicking phantom across the horizontal yellow line in Fig. 6(a) calculated by GLUE and CGLUE. Windows of length 3, 35 and 65 are used for estimating strain by LSQ in (a), (b) and (c), respectively.

TABLE II: Bias and variance of strain estimation error for different levels of noise for 4-layers uniform simulation study. For each level of noise, the experiment is repeated 100 times and the reported values in this table are averages of all experiments.

SNR (dB)		Bias	Variance
∞	GLUE	30.45×10^{-5}	3.20×10^{-5}
	CGLUE	-2.64×10^{-5}	2.94×10^{-5}
40	GLUE	30.51×10^{-5}	3.21×10^{-5}
	CGLUE	-3.90×10^{-5}	2.98×10^{-5}
30	GLUE	30.79×10^{-5}	3.26×10^{-5}
	CGLUE	-4.33×10^{-5}	2.92×10^{-5}
25	GLUE	46.34×10^{-5}	3.63×10^{-5}
	CGLUE	17.08×10^{-5}	3.04×10^{-5}

and 65. CGLUE provides a lower variance strain error estimation than that of GLUE in all cases. This is important as the background and inclusions of the experimental phantoms are uniform and linear elastic materials. Moreover, the smoother strain field of CGLUE for $\rho = 3$ shows that the corresponding TDE profile has lower variance than TDE profile for GLUE. The ESF profiles that are calculated across the yellow line in Fig. 6 (a) are also shown in Fig. 7. Fig. 7 clarifies that CGLUE exhibits better performance than GLUE for all LSQ window sizes by generating smoother results. The length of LSQ windows do not impact results of CGLUE as much as GLUE, which implies a less noisy TDE field by CGLUE. To make sure that low variance strain error estimation does not result in a large bias error, the CNR is utilized to show the contrast between lesion and background. The calculated CNRs are reported in Table III.

TABLE III: CNR for strain images of the phantom data for different methods. Windows that are considered for calculating CNR are shown in red and blue lines in Fig. 6.

ρ		CNR (dB)
3	GLUE	4.54 (6.58)
	CGLUE	5.39 (7.32)
	Improvement	$\mathbf{18.72\%(11.24\%)}$
35	GLUE	4.69 (6.72)
	CGLUE	5.44 (7.36)
	Improvement	$\mathbf{15.99\%(9.52\%)}$
65	GLUE	4.81 (6.83)
	CGLUE	5.50 (7.41)
	Improvement	$\mathbf{14.34\%(8.49\%)}$

TABLE IV: CNR for strain images of the *ex-vivo* data for different methods. Windows that are considered for calculating CNR are shown in white and black lines in Fig. 8.

ρ		CNR (dB)
3	GLUE	10.20 (10.09)
	CGLUE	31.76 (15.02)
	Improvement	$\mathbf{211.37\%(45.22\%)}$
35	GLUE	20.09 (13.03)
	CGLUE	49.88 (16.98)
	Improvement	$\mathbf{148.28\%(30.31\%)}$
65	GLUE	28.84 (14.60)
	CGLUE	63.24 (18.01)
	Improvement	$\mathbf{119.27\%(23.35\%)}$

ex-vivo Results

Similar to the previous sections, three different windows are considered for estimating strain. The windows of LSQ have sizes of 3, 35 and 65. CGLUE displays the olive piece more clearly than GLUE by providing a higher contrast and lower noise in the background.

The ESFs of the estimated strains across the vertical line in Fig. 8 (a) are also shown in Fig. 9. According to Fig. 9, the TDE field obtained from CGLUE is much less noisy than the TDE field obtained from GLUE, since the resulted strain of CGLUE with $\rho = 3$ is smoother than the strain of GLUE. Meanwhile, strain of CGLUE with $\rho = 35, 65$ are smoother than GLUE.

For quantitative comparison of CGLUE and GLUE, the calculated CNRs are reported in Table IV. The improvement of CGLUE with respect to GLUE in this experiment is much more than simulation and phantom experiments due to high level of noise that is present in *ex-vivo* data.

IV. Discussion

In this paper, a method named CGLUE is proposed for ultrasound elastography. CGLUE can be used for displacement estimation in other elastography techniques such as ARFI [29] and shear-wave elastography [31]. The estimated displacement by CGLUE is more accurate than other approaches such as GLUE. To avoid repetition we restrict our comparison to CGLUE and GLUE since our previous work [1] already illustrates the superior performance of GLUE over window-based methods. In addition, this comparison directly focuses on the advantage of utilizing pre-beamformed channel data since that is the only difference between GLUE and CGLUE. The lower bias and variance of error in the estimated displacement is important since strain fields are calculated by differentiating displacement fields which amplifies the noise.

The cost function proposed in CGLUE consist of two parts. The first part (data term) penalizes pre- and post-compressed images. The novelty of CGLUE is using time-gain and time-delay corrected channel data instead of RF data. The channel data contains more information than RF data which intuitively informs that their comparison results in better displacement estimation than RF data. We also prove that utilizing channel data in data term decreases bias and variance of error. The main difference of data term for GLUE and CGLUE is that for GLUE, the data from all channels are summed up and all operations are implemented on it. However, for CGLUE, all operations are done individually on separate channels and their summation is considered in the final solution. This means that for a coherent target such as a point reflector, CGLUE and GLUE yield the same result, assuming no noise. For speckle targets, the comparison is more interesting as GLUE suffers more from speckle decorrelation especially with large deformations. Off axis scattering, thermal noise, and decorrelation due to scatterer shift are most common noises in ultrasound imaging [59], [65]–[67]. Other sources of noises that are related to free-hand elastography is the out-of-plane motion in images and heat generated in the ablation procedures.

The second term of cost function deals with regularization which penalizes a quadratic term of displacement differences for neighbor samples. In the regularization term used in [1], the difference between $a_{i,j} + \Delta a_{i,j}$ and $a_{i-1,j} - \Delta a_{i-1,j}$ are penalized which makes the TDE smoother by decreasing the variance at cost of increased bias. To decrease the underestimated displacement estimation, ε_a and ε_l are considered in the regularization term of CGLUE as proposed in [55], [56], where ε_a is the average of integer axial displacement difference between subsequent samples i and $i-1$ and ε_l is the average of integer lateral displacement difference between samples j and $j-1$ which are available from DP. Comparing results of GLUE with CGLUE in Figs. 6 and 8, it is clear that the underestimation at the top and bottom of strain fields are resolved by adding this term.

CGLUE is dealing with large matrices of size $2mn \times 2mn$. For a typical RF frame of size 1000×100, this matrix will be of size 200000×200000 needing 298 GB of memory for storage in double precision floating point format. Fortunately, most elements of these matrices are zero, and as such, they can be stored as sparse matrices to reduce memory load. As an example, left hand side of Eq. (6) for a typical RF frame of size 1000×100 needs only 19.73 MB and the right hand side uses 1.52 MB of memory, if they are stored as sparse matrices. The CGLUE code is currently implemented in Matlab and

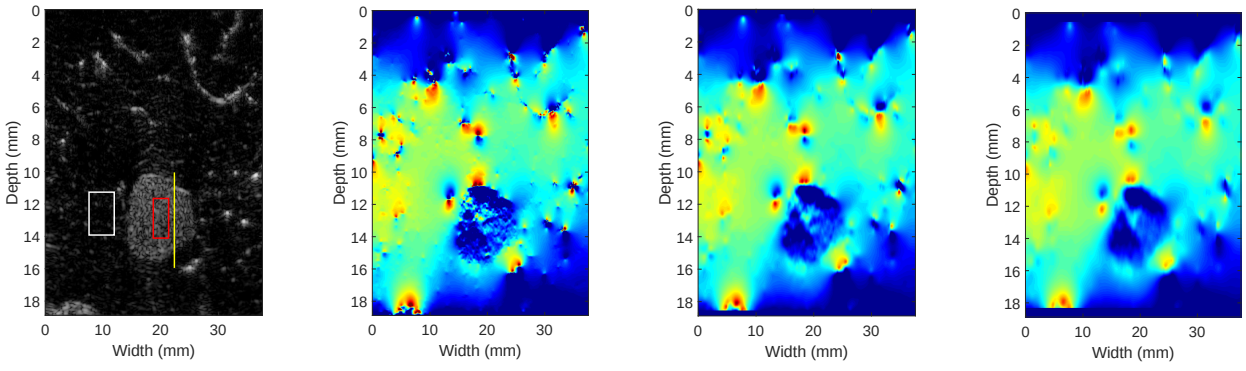

(a) B-mode (b) GLUE, $\rho = 3$ (c) GLUE, $\rho = 35$ (d) GLUE, $\rho = 65$

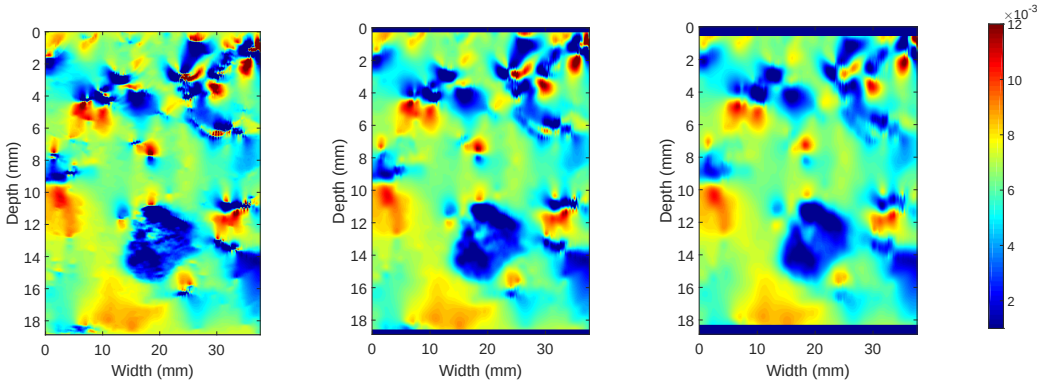

(e) CGLUE, $\rho = 3$ (f) CGLUE, $\rho = 35$ (g) CGLUE, $\rho = 65$

Fig. 8: B-mode image of the lamb liver with small piece of olive placed in (a). Estimated strain images using GLUE and CGLUE for different LSQ window sizes are shown in (b)-(g). Note that the CGLUE result in (e) is less noisy despite a small value for ρ.

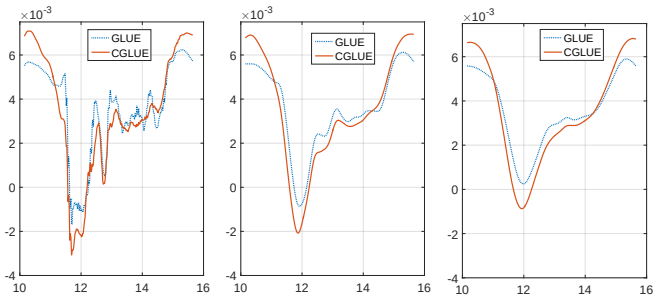

(a) $\rho = 3$ (b) $\rho = 35$ (c) $\rho = 65$

Fig. 9: Strain profiles of the liver data across the vertical yellow line in Fig. 8(a) calculated by GLUE and CGLUE. Windows of length 3, 35 and 65 are used for estimating strain by LSQ in (a), (b) and (c), respectively.

takes 2.4 seconds on a 3.20 GHz i7 Intel CPU for an image of size 1000×100 which is collected by 64 channels. By implementing CGLUE in C and using graphics cards, it can achieve real-time performance.

APPENDIX

The matrices of Eq. (6) is provided in this appendix. The matrix V is a $2mn \times 2mn$ matrix as

$$V = \begin{bmatrix} Q & R & 0 & & & & \\ R & S & R & 0 & & 0 & \\ 0 & R & S & R & 0 & & \\ & \ddots & & \ddots & & \ddots & \\ & & 0 & R & S & R & 0 \\ & 0 & & \ddots & R & S & R \\ & & & & 0 & R & Q \end{bmatrix}$$

in which Q, S are pentadiagonal matrices as shown in Eqs. (19), (20) and R is a diagonal matrix as

$$R = \text{diag}\{-\alpha_1, -\beta_1, \cdots, -\alpha_1, -\beta_1\}.$$

The matrix H is a diagonal matrix as

$$H = \text{diag}\{h(1,1), \cdots, h(1,n), \cdots, h(m,1), \cdots, h(m,n)\}$$

where $h(i,j)$ is a 2×2 matrix as

$$h(i,j) = \frac{1}{c} \begin{bmatrix} \sum_{k=1}^{c} (I'_{2a}(.))^2 & \sum_{k=1}^{c} (I'_{2a}(.) I'_{2l}(.)) \\ \sum_{k=1}^{c} (I'_{2a}(.) I'_{2l}(.)) & \sum_{k=1}^{c} (I'_{2l}(.))^2 \end{bmatrix}.$$

P is a diagonal matrix given by

$$P = \text{diag}\{e(1,1), \cdots, e(1,n), \cdots, e(m,1), \cdots, e(m,n)\}.$$

$e(i,j)$ is a matrix of size 2×2 as

$$e(i,j) = \begin{bmatrix} I'_{2a}(.) & 0 \\ 0 & I'_{2l}(.) \end{bmatrix}.$$

μ is a vector as

$$\mu = [g_{1,1}, g_{1,2}, \cdots, g_{m,n}]^{\mathrm{T}} \otimes [1,1]^{\mathrm{T}},$$

$g_{i,j}$ is difference of two images as

$$g_{i,j} = I_1(i+k, j+r) - I_2(.)$$

and $\otimes$ is Kronecker tensor product.

The vector d contains integer displacements as

$$d = [a_{11}, l_{11}, a_{12}, l_{12}, \cdots, a_{mn}, l_{mn}]^{\mathrm{T}}$$

and finally the vector b is a $mn \times mn$ vector as

$$b = [1, 0, \cdots, 0, -1]^{\mathrm{T}}.$$

$$Q = \begin{bmatrix} \alpha_1+\alpha_2 & 0 & -\alpha_2 & 0 & & & & & \\ 0 & \beta_1+\beta_2 & 0 & -\beta_2 & 0 & & & \mathbf{0} & \\ -\alpha_2 & 0 & \alpha_1+2\alpha_2 & 0 & -\alpha_2 & 0 & & & \\ 0 & -\beta_2 & 0 & \beta_1+2\beta_2 & 0 & -\beta_2 & 0 & & \\ & \ddots & \ddots & & \ddots & & \ddots & \ddots & \\ & & 0 & -\alpha_2 & 0 & \alpha_1+2\alpha_2 & 0 & -\alpha_2 & 0 \\ & & & 0 & -\beta_2 & 0 & \beta_1+2\beta_2 & 0 & -\beta_2 \\ & \mathbf{0} & & & 0 & -\alpha_2 & 0 & \alpha_1+\alpha_2 & 0 \\ & & & & & 0 & -\beta_2 & 0 & \beta_1+\beta_2 \end{bmatrix} \tag{19}$$

$$S = \begin{bmatrix} 2\alpha_1+\alpha_2 & 0 & -\alpha_2 & 0 & & & & & \\ 0 & 2\beta_1+\beta_2 & 0 & -\beta_2 & 0 & & & \mathbf{0} & \\ -\alpha_2 & 0 & 2\alpha_1+2\alpha_2 & 0 & -\alpha_2 & 0 & & & \\ 0 & -\beta_2 & 0 & 2\beta_1+2\beta_2 & 0 & -\beta_2 & 0 & & \\ & \ddots & \ddots & & \ddots & & \ddots & \ddots & \\ & & 0 & -\alpha_2 & 0 & 2\alpha_1+2\alpha_2 & 0 & -\alpha_2 & 0 \\ & & & 0 & -\beta_2 & 0 & 2\beta_1+2\beta_2 & 0 & -\beta_2 \\ & \mathbf{0} & & & 0 & -\alpha_2 & 0 & 2\alpha_1+\alpha_2 & 0 \\ & & & & & 0 & -\beta_2 & 0 & 2\beta_1+\beta_2 \end{bmatrix} \tag{20}$$

ACKNOWLEDGMENT

This work was supported by Natural Science and Engineering Research Council of Canada (NSERC) Discovery Grants RGPIN-04136 and RGPIN-2017-06629. The data of mimicking phantom and *ex-vivo* were collected at Concordia University's PERFORM Centre with an Alpinion ultrasound machine.

REFERENCES

[1] H. S. Hashemi and H. Rivaz, "Global time-delay estimation in ultrasound elastography," *IEEE Transactions on Ultrasonics, Ferroelectrics, and Frequency Control*, vol. 64, no. 10, pp. 1625–1636, 2017.

[2] R. Sinkus, J. Lorenzen, D. Schrader, M. Lorenzen, M. Dargatz, and D. Holz, "High-resolution tensor mr elastography for breast tumour detection," *Physics in Medicine & Biology*, vol. 45, no. 6, p. 1649, 2000.

[3] O. Rouviere, M. Yin, M. A. Dresner, P. J. Rossman, L. J. Burgart, J. L. Fidler, and R. L. Ehman, "Mr elastography of the liver: preliminary results," *Radiology*, vol. 240, no. 2, pp. 440–448, 2006.

[4] J. Ophir, I. Cespedes, H. Ponnekanti, Y. Yazdi, and X. Li, "Elastography: a quantitative method for imaging the elasticity of biological tissues," *Ultrasonic imaging*, vol. 13, no. 2, pp. 111–134, 1991.

[5] A. Sarvazyan, T. J Hall, M. W Urban, M. Fatemi, S. R Aglyamov, and B. S Garra, "An overview of elastography-an emerging branch of medical imaging," *Current medical imaging reviews*, vol. 7, no. 4, pp. 255–282, 2011.

[6] P. N. T. Wells, "Ultrasound imaging," *Physics in Medicine and Biology*, vol. 51, no. 13, pp. R83–R98, 2006.

[7] R. M. Sigrist, J. Liau, A. El Kaffas, M. C. Chammas, and J. K. Willmann, "Ultrasound elastography: review of techniques and clinical applications," *Theranostics*, vol. 7, no. 5, p. 1303, 2017.

[8] Y. Hong, X. Liu, Z. Li, X. Zhang, M. Chen, and Z. Luo, "Real-time ultrasound elastography in the differential diagnosis of benign and malignant thyroid nodules," *Journal of Ultrasound in Medicine*, vol. 28, no. 7, pp. 861–867, 2009.

[9] P. Trimboli, R. Guglielmi, S. Monti, I. Misischi, F. Graziano, N. Nasrollah, S. Amendola, S. N. Morgante, M. G. Deiana, S. Valabrega *et al.*, "Ultrasound sensitivity for thyroid malignancy is increased by real-time elastography: a prospective multicenter study," *The Journal of Clinical Endocrinology & Metabolism*, vol. 97, no. 12, pp. 4524–4530, 2012.

[10] A. E. Samir, M. Dhyani, A. Anvari, J. Prescott, E. F. Halpern, W. C. Faquin, and A. Stephen, "Shear-wave elastography for the preoperative risk stratification of follicular-patterned lesions of the thyroid: diagnostic

accuracy and optimal measurement plane," *Radiology*, vol. 277, no. 2, pp. 565–573, 2015.

[11] T. J. Hall, Y. Zhu, C. S. Spalding, and L. T. Cook, "In vivo results of real-time freehand elasticity imaging," in *2001 IEEE Ultrasonics Symposium. Proceedings. An International Symposium (Cat. No. 01CH37263)*, vol. 2. IEEE, 2001, pp. 1653–1657.

[12] M. M. Doyley, J. C. Bamber, F. Fuechsel, and N. L. Bush, "A freehand elastographic imaging approach for clinical breast imaging: system development and performance evaluation," *Ultrasound in medicine & biology*, vol. 27, no. 10, pp. 1347–1357, 2001.

[13] N. Uniyal, H. Eskandari, P. Abolmaesumi, S. Sojoudi, P. Gordon, L. Warren, R. N. Rohling, S. E. Salcudean, and M. Moradi, "Ultrasound rf time series for classification of breast lesions," *IEEE transactions on medical imaging*, vol. 34, no. 2, pp. 652–661, 2015.

[14] H. Rivaz, E. M. Boctor, M. A. Choti, and G. D. Hager, "Ultrasound elastography using multiple images," *Medical image analysis*, vol. 18, no. 2, pp. 314–329, 2014.

[15] W. Yang, M. Alexander, N. Rubert, A. Ingle, M. Lubner, T. Ziemlewicz, J. Hinshaw, F. Lee, J. Zagzebski, and T. Varghese, "Monitoring microwave ablation for liver tumors with electrode displacement strain imaging," in *2014 IEEE International Ultrasonics Symposium*. IEEE, 2014, pp. 1128–1131.

[16] N. Frulio and H. Trillaud, "Ultrasound elastography in liver," *Diagnostic and Interventional Imaging*, vol. 94, no. 5, pp. 515 – 534, 2013.

[17] S. Selladurai and A. K. Thittai, "Towards quantitative quasi-static ultrasound elastography using a reference layer for liver imaging application: A preliminary assessment," *Ultrasonics*, vol. 93, pp. 7–17, 2019.

[18] M. Friedrich-Rust, M.-F. Ong, S. Martens, C. Sarrazin, J. Bojunga, S. Zeuzem, and E. Herrmann, "Performance of transient elastography for the staging of liver fibrosis: a meta-analysis," *Gastroenterology*, vol. 134, no. 4, pp. 960–974, 2008.

[19] E. Tsochatzis, K. Gurusamy, S. Ntaoula, E. Cholongitas, B. Davidson, and A. Burroughs, "Elastography for the diagnosis of severity of fibrosis in chronic liver disease: a meta-analysis of diagnostic accuracy," *Journal of hepatology*, vol. 54, no. 4, pp. 650–659, 2011.

[20] A. Lorenz, H. Sommerfeld, M. Garcia-Schurmann, S. Philippou, T. Senge, and H. Ermert, "A new system for the acquisition of ultrasonic multicompression strain images of the human prostate in vivo," *ieee transactions on ultrasonics, ferroelectrics, and frequency control*, vol. 46, no. 5, pp. 1147–1154, 1999.

[21] J. Correas, E. Drakonakis, A. Isidori, O. Hélénon, C. Pozza, V. Cantisani, N. Di Leo, F. Maghella, A. Rubini, F. Drudi *et al.*, "Update on ultrasound elastography: miscellanea. prostate, testicle, musculo-skeletal," *European journal of radiology*, vol. 82, no. 11, pp. 1904–1912, 2013.

[22] A. Săftoiu and P. Vilman, "Endoscopic ultrasound elastography-a new imaging technique for the visualization of tissue elasticity distribution," *Journal of Gastrointestinal and Liver Diseases*, vol. 15, no. 2, p. 161, 2006.

[23] T. Selbekk, J. Bang, and G. Unsgaard, "Strain processing of intraoperative ultrasound images of brain tumours: initial results," *Ultrasound in medicine & biology*, vol. 31, no. 1, pp. 45–51, 2005.

[24] T. Selbekk, R. Brekken, O. Solheim, S. Lydersen, T. A. Hernes, and G. Unsgaard, "Tissue motion and strain in the human brain assessed by intraoperative ultrasound in glioma patients," *Ultrasound in medicine & biology*, vol. 36, no. 1, pp. 2–10, 2010.

[25] A. Skovoroda, S. Emelianov, and M. O'donnell, "Tissue elasticity reconstruction based on ultrasonic displacement and strain images," *IEEE transactions on ultrasonics, ferroelectrics, and frequency control*, vol. 42, no. 4, pp. 747–765, 1995.

[26] X. Pan, K. Liu, J. Bai, and J. Luo, "A regularization-free elasticity reconstruction method for ultrasound elastography with freehand scan," *Biomedical engineering online*, vol. 13, no. 1, p. 132, 2014.

[27] J. Bercoff, M. Tanter, and M. Fink, "Supersonic shear imaging: a new technique for soft tissue elasticity mapping," *IEEE transactions on ultrasonics, ferroelectrics, and frequency control*, vol. 51, no. 4, pp. 396–409, 2004.

[28] T. Gallot, S. Catheline, P. Roux, J. Brum, N. Benech, and C. Negreira, "Passive elastography: shear-wave tomography from physiological-noise correlation in soft tissues," *IEEE transactions on ultrasonics, ferroelectrics, and frequency control*, vol. 58, no. 6, pp. 1122–1126, 2011.

[29] K. Nightingale, S. McAleavey, and G. Trahey, "Shear-wave generation using acoustic radiation force: in vivo and ex vivo results," *Ultrasound in medicine & biology*, vol. 29, no. 12, pp. 1715–1723, 2003.

[30] D. M. Dumont and B. C. Byram, "Robust tracking of small displacements with a bayesian estimator," *IEEE transactions on ultrasonics, ferroelectrics, and frequency control*, vol. 63, no. 1, pp. 20–34, 2015.

[31] L. Sandrin, M. Tanter, J.-L. Gennisson, S. Catheline, and M. Fink, "Shear elasticity probe for soft tissues with 1-d transient elastography," *IEEE transactions on ultrasonics, ferroelectrics, and frequency control*, vol. 49, no. 4, pp. 436–446, 2002.

[32] G. Treece, J. Lindop, L. Chen, J. Housden, R. Prager, and A. Gee, "Real-time quasi-static ultrasound elastography," *Interface focus*, vol. 1, no. 4, pp. 540–552, 2011.

[33] C. Schneider, A. Baghani, R. Rohling, and S. Salcudean, "Remote ultrasound palpation for robotic interventions using absolute elastography," in *International Conference on Medical Image Computing and Computer-Assisted Intervention*. Springer, 2012, pp. 42–49.

[34] T. Adebar, S. Salcudean, S. Mahdavi, M. Moradi, C. Nguan, and L. Goldenberg, "A robotic system for intra-operative trans-rectal ultrasound and ultrasound elastography in radical prostatectomy," in *International Conference on Information Processing in Computer-Assisted Interventions*. Springer, 2011, pp. 79–89.

[35] R. Xia, G. Tao, and A. Thittai, "Dynamic frame pairing in real-time freehand elastography," *IEEE transactions on ultrasonics, ferroelectrics, and frequency control*, vol. 61, no. 6, pp. 979–985, 2014.

[36] T. J. Hall, Y. Zhu, and C. S. Spalding, "In vivo real-time freehand palpation imaging," *Ultrasound in medicine & biology*, vol. 29, no. 3, pp. 427–435, 2003.

[37] S. Bharat, T. Varghese, E. L. Madsen, and J. A. Zagzebski, "Radio-frequency ablation electrode displacement elastography: A phantom study," *Medical physics*, vol. 35, no. 6Part1, pp. 2432–2442, 2008.

[38] A. Bruhn, J. Weickert, and C. Schnörr, "Lucas/kanade meets horn/schunck: Combining local and global optic flow methods," *International journal of computer vision*, vol. 61, no. 3, pp. 211–231, 2005.

[39] T. Varghese, E. Konofagou, J. Ophir, S. Alam, and M. Bilgen, "Direct strain estimation in elastography using spectral cross-correlation," *Ultrasound in medicine & biology*, vol. 26, no. 9, pp. 1525–1537, 2000.

[40] M. Mirzaei, A. Asif, M. Fortin, and H. Rivaz, "3d normalized cross-correlation for estimation of the displacement field in ultrasound elastography," *Ultrasonics*, vol. 102, p. 106053, 2020.

[41] R. Zahiri-Azar and S. E. Salcudean, "Motion estimation in ultrasound images using time domain cross correlation with prior estimates." *IEEE Trans. Biomed. Engineering*, vol. 53, no. 10, pp. 1990–2000, 2006.

[42] L. Yuan and P. C. Pedersen, "Analytical phase-tracking-based strain estimation for ultrasound elasticity," *IEEE transactions on ultrasonics, ferroelectrics, and frequency control*, vol. 62, no. 1, pp. 185–207, 2015.

[43] P. Chaturvedi, M. F. Insana, and T. J. Hall, "Testing the limitations of 2-d companding for strain imaging using phantoms," *IEEE transactions on ultrasonics, ferroelectrics, and frequency control*, vol. 45, no. 4, pp. 1022–1031, 1998.

[44] M. G. Kibria and H. Rivaz, "Gluenet: ultrasound elastography using convolutional neural network," in *Simulation, Image Processing, and Ultrasound Systems for Assisted Diagnosis and Navigation*. Springer, 2018, pp. 21–28.

[45] Z. Gao, S. Wu, Z. Liu, J. Luo, H. Zhang, M. Gong, and S. Li, "Learning the implicit strain reconstruction in ultrasound elastography using privileged information," *Medical image analysis*, vol. 58, p. 101534, 2019.

[46] B. Peng, Y. Xian, Q. Zhang, and J. Jiang, "Neural-network-based motion tracking for breast ultrasound strain elastography: An initial assessment of performance and feasibility," *Ultrasonic Imaging*, vol. 42, no. 2, pp. 74–91, 2020.

[47] A. K. Tehrani and H. Rivaz, "Displacement estimation in ultrasound elastography using pyramidal convolutional neural network," *IEEE Transactions on Ultrasonics, Ferroelectrics, and Frequency Control*, 2020.

[48] T. J Hall, P. E Barboneg, A. A Oberai, J. Jiang, J.-F. Dord, S. Goenezen, and T. G Fisher, "Recent results in nonlinear strain and modulus imaging," *Current medical imaging reviews*, vol. 7, no. 4, pp. 313–327, 2011.

[49] C. Pellot-Barakat, F. Frouin, M. F. Insana, and A. Herment, "Ultrasound elastography based on multiscale estimations of regularized displacement fields," *IEEE transactions on medical imaging*, vol. 23, no. 2, pp. 153–163, 2004.

[50] E. Brusseau, J. Kybic, J.-F. Déprez, and O. Basset, "2-d locally regularized tissue strain estimation from radio-frequency ultrasound images: Theoretical developments and results on experimental data," *IEEE Transactions on Medical Imaging*, vol. 27, no. 2, pp. 145–160, 2008.

[51] A. Kuzmin, A. M. Zakrzewski, B. W. Anthony, and V. Lempitsky, "Multi-frame elastography using a handheld force-controlled ultrasound probe," *IEEE transactions on ultrasonics, ferroelectrics, and frequency control*, vol. 62, no. 8, pp. 1486–1500, 2015.

[52] L. Guo, Y. Xu, Z. Xu, and J. Jiang, "A pde-based regularization algorithm toward reducing speckle tracking noise: A feasibility study for ultrasound breast elastography," *Ultrasonic imaging*, vol. 37, no. 4, pp. 277–293, 2015.

[53] X. Pan, J. Gao, S. Tao, K. Liu, J. Bai, and J. Luo, "A two-step optical flow method for strain estimation in elastography: Simulation and phantom study," *Ultrasonics*, vol. 54, no. 4, pp. 990–996, 2014.

[54] H. Rivaz, E. Boctor, P. Foroughi, R. Zellars, G. Fichtinger, and G. Hager, "Ultrasound elastography: a dynamic programming approach," *IEEE transactions on medical imaging*, vol. 27, no. 10, pp. 1373–1377, 2008.

[55] H. Rivaz, E. M. Boctor, M. A. Choti, and G. D. Hager, "Real-time regularized ultrasound elastography," *IEEE transactions on medical imaging*, vol. 30, no. 4, pp. 928–945, 2011.

[56] M. Mirzaei, A. Asif, and H. Rivaz, "Combining total variation regularization with window-based time delay estimation in ultrasound elastography," *IEEE Transactions on Medical Imaging*, vol. 38, no. 12, pp. 2744–2754, 2019.

[57] C. E. Shannon, "Communication in the presence of noise," *Proceedings of the IEEE*, vol. 86, no. 2, pp. 447–457, 1998.

[58] M. Mirzaei, A. Asif, and H. Rivaz, "Ultrasound elastography utilizing pre-beam-formed data," in *IEEE International Symposium on Biomedical Imaging (ISBI)*, 2019.

[59] W. Long, N. Bottenus, and G. E. Trahey, "Lag-one coherence as a metric for ultrasonic image quality," *IEEE transactions on ultrasonics, ferroelectrics, and frequency control*, vol. 65, no. 10, pp. 1768–1780, 2018.

[60] M. A. Kutay, A. P. Petropulu, and C. W. Piccoli, "On modeling biomedical ultrasound rf echoes using a power-law shot-noise model," *IEEE transactions on ultrasonics, ferroelectrics, and frequency control*, vol. 48, no. 4, pp. 953–968, 2001.

[61] T. Varghese and J. Ophir, "An analysis of elastographic contrast-to-noise ratio," *Ultrasound in medicine & biology*, vol. 24, no. 6, pp. 915–924, 1998.

[62] J. Ophir, S. K. Alam, B. Garra, F. Kallel, E. Konofagou, T. Krouskop, and T. Varghese, "Elastography: ultrasonic estimation and imaging of the elastic properties of tissues," *Proceedings of the Institution of Mechanical Engineers, Part H: Journal of Engineering in Medicine*, vol. 213, no. 3, pp. 203–233, 1999.

[63] J. Jensen, "Field: A program for simulating ultrasound systems," *Medical and Biological Engineering and Computing*, vol. 34, pp. 351–352, 01 1996.

[64] J. A. Jensen and N. B. Svendsen, "Calculation of pressure fields from arbitrarily shaped, apodized, and excited ultrasound transducers," *IEEE Transactions on Ultrasonics, Ferroelectrics, and Frequency Control*, vol. 39, no. 2, pp. 262–267, 1992.

[65] D. Zhao, L. Bohs, and G. Trahey, "Phase aberration correction using echo signals from moving targets i: Description and theory," *Ultrasonic imaging*, vol. 14, no. 2, pp. 97–110, 1992.

[66] S. Krishnan, K. Rigby, and M. O'donnell, "Adaptive aberration correction of abdominal images using parca," *Ultrasonic imaging*, vol. 19, no. 3, pp. 169–179, 1997.

[67] J. Mann and W. Walker, "A constrained adaptive beamformer for medical ultrasound: Initial results," in *2002 IEEE Ultrasonics Symposium, 2002. Proceedings.*, vol. 2. IEEE, 2002, pp. 1807–1810.

Morteza Mirzaei received his BSc degree from Tabriz University and MASc from Amirkabir University of Technology, Tehran, Iran. He is currently pursuing his PhD in electrical and computer engineering at IMPACT lab at Concordia University, Montreal, Canada. His research interest are medical image analysis, ultrasound imaging and elastography.

Amir Asif (M'97–SM'02) received the M.Sc. and Ph.D. degrees in electrical and computer engineering from Carnegie Mellon University (CMU), Pittsburgh, PA in 1993 and 1996, respectively. He has been a professor of electrical and computer engineering at Concordia University since 2014, where he is now serving as the Dean of the Faculty of Engineering and Computer Science. Previously, he was a professor of electrical engineering and computer science at York University, Toronto, ON, Canada, from 2002 to 2014 and on the faculty of CMU, where he was a Research Engineer from 1997 to 1999.

Asif works in the area of statistical signal processing and communications. His current projects include distributed agent networks (autonomy and consensus in complex and contested environments); medical imaging (ultrasound elastography, brain computer interfaces), data science (graph signal processing in social networks); and health management of mission critical systems. He has authored over 175 technical contributions, including invited ones, published in international journals and conference proceedings, and a textbook "Continuous and Discrete Time Signals and Systems" published by the Cambridge University Press.

Asif has served on the editorial boards of numerous journals and international conferences, including Associate Editor for IEEE Transactions of Signal Processing (2014-18), IEEE Signal Processing letters (2002-2006, 2009-2013). He has organized a number of IEEE conferences on signal processing theory and applications. He has received several distinguishing awards including the York University Faculty of Graduate Studies Teaching Award in 2008; York University Wide Teaching Award (Full-Time Senior Faculty Category) in 2008 from York University; the FSE Teaching Excellence Award (Senior Faculty Category) from York's Faculty of Science and Engineering in 2006 and in 2004; and the CSE Mildred Baptist Teaching Excellence Award from York's Department of Computer Science and Engineering in 2006 and in 2003. He is a member of the Professional Engineering Society of Ontario and a senior member of IEEE.

Hassan Rivaz received BSc degree from Sharif University of Technology, MASc from the University of British Columbia, and PhD from Johns Hopkins University.

He directs the IMPACT lab: IMage Processing And Characterization of Tissue, and is a Concordia University Research Chair in Medical Image Analysis. His research interests are medical image analysis, machine learning, deep learning, elastography and quantitative ultrasound.

He is an Associate Editor of IEEE Transactions on Medical Imaging (TMI), and IEEE Transactions on Ultrasonics, Ferroelectrics and Frequency Control (TUFFC). He is a member of the Organizing Committee of IEEE EMBC 2020 (Montreal, Canada), IEEE ISBI 2021 (Nice, France), and IEEE IUS 2023 (Montreal, Canada).

He has served as an Area Chair of MICCAI since 2017. He co-organized two tutorials on advances in ultrasound imaging at IEEE ISBI 2019 and 2018. He also co-organized the CURIOUS 2018 and CURIOUS 2019 Challenges on registration of ultrasound and MRI in neurosurgery, and the CereVis 2018 Workshop on Cerebral Data Visualization, all in conjunction with MICCAI. He was a Petro-Canada Young Innovator from 2016 to 2018.